Droplets, Bubbles and Ultrasound Interactions

9

Oleksandr Shpak, Martin Verweij, Nico de Jong, and Michel Versluis

Abstract

The interaction of droplets and bubbles with ultrasound has been studied extensively in the last 25 years. Microbubbles are broadly used in diagnostic and therapeutic medical applications, for instance, as ultrasound contrast agents. They have a similar size as red blood cells, and thus are able to circulate within blood vessels. Perfluorocarbon liquid droplets can be a potential new generation of microbubble agents as ultrasound can trigger their conversion into gas bubbles. Prior to activation, they are at least five times smaller in diameter than the resulting bubbles. Together with the violent nature of the phase-transition, the droplets can be used for local drug delivery, embolotherapy, HIFU enhancement and tumor imaging. Here we explain the basics of bubble dynamics, described by the Rayleigh-Plesset equation, bubble resonance frequency, damping and quality factor. We show the elegant calculation of the above characteristics for the case of small amplitude oscillations by linearizing the equations. The effect and importance of a bubble coating and effective surface tension are also discussed. We give the main characteristics of the power spectrum of bubble oscillations. Preceding bubble dynamics, ultrasound propagation is introduced. We explain the speed of sound, nonlinearity and attenuation terms. We examine bubble ultrasound scattering and how it depends on the wave-shape of the incident wave. Finally, we introduce droplet

O. Shpak • M. Versluis (✉)
Physics of Fluids Group,
MIRA Institute for Biomedical Technology and
Technical Medicine, University of Twente,
P.O. Box 217, Enschede 7500 AE, The Netherlands
e-mail: m.versluis@utwente.nl

M. Verweij
Acoustic Wavefield Imaging, Delft University
of Technology, Delft 2600 GA, The Netherlands

N. de Jong
Acoustic Wavefield Imaging,
Delft University of Technology, Delft 2600 GA,
The Netherlands

Biomedical Engineering,
Erasmus MC University Medical Center Rotterdam,
Rotterdam 3000 CA, The Netherlands

interaction with ultrasound. We elucidate the ultrasound-focusing concept within a droplets sphere, droplet shaking due to media compressibility and droplet phase-conversion dynamics.

Keyword

Droplet • Microbubble • Ultrasound

9.1   Introduction

Medical ultrasound is widely used for imaging purposes (Szabo 2004). It is an effective, mobile, inexpensive method and has the ability to provide high-resolution real-time images of tissue (Shung 2006). Ultrasound imaging is performed by propagating waves through tissue and evaluating the echo that is returned. Due to the different scattering properties of the different tissues, the ultrasound receiver can evaluate the echo and construct an acoustic image.

The ultrasound wave is transmitted by an ultrasound transducer. It consists of piezoelectric crystals, which have the property of changing their volume when a voltage is applied. Applying an alternating current across piezoelectric crystals causes them to volumetrically oscillate at frequencies (∼MHz) that cause mechanical stress on the surrounding medium, thereby converting electric energy into a mechanical wave, which is then transmitted into the body. Analogously, upon receiving the echo the transducer turns the mechanical sound waves back into electrical energy, which can be measured and displayed. The transmit signal consists of a short ultrasound burst. After each burst, the electronics measure the return signal within a small window of time corresponding to the time it takes for the energy to pass through the tissue.

Blood is a poor ultrasound scatterer and individual blood vessels are almost invisible to ultrasound. To increase the contrast of the blood pool, microbubbles can be injected into the bloodstream. The microbubbles scatter ultrasound much more efficiently, allowing very good contrast on the echo image. The contrast ability was discovered accidentally more than 40 years ago during an intravenous injection of a saline solution (Gramiak and Shah 1968). Saline, when injected intravenously, generates tiny microbubbles within the patient's blood vessels, thus creating an echo on the acoustic image. Since then, the second and third generations of ultrasound contrast agents were developed. Nowadays, commercially available microbubbles are small spheres (typically 1–5 μm in diameter) of gas encapsulated in a biocompatible shell. This size is similar to that of red blood cells, allowing them to circulate inside the bloodstream. The resonance frequency is directly related to the size of the bubbles (1–10 μm diameter) and coincides with the optimum imaging frequencies used in medical ultrasound imaging, 1–10 MHz.

Microbubbles are also widely used for therapy. They can enhance high intensity focused ultrasound (HIFU) therapy (Unger et al. 2004). The bubbles increase heat uptake by the tissue and can reduce the time necessary for an ultrasound therapeutic procedure. They are sufficiently stable for time periods of approximately 15 min following injection (Klibanov 2006). Bubble oscillations and disruptions close to cells create reversible pores within the cell membrane that can enhance drug uptake (Karshafian et al. 2009). Microbubbles may also be used as potential carriers for selective drug delivery (Unger et al. 2009) and for non-invasive molecular imaging (Lindner 2004; Klibanov 2006). They can be covered with targeting ligands, such as antibodies, which bind specifically to target cells at the blood vessel wall.

A novel approach is the use of liquid-based agents rather than gas bubbles. Ultrasound can be used to phase-transition these liquid droplets into gas bubbles; a process known as acoustic droplet vaporization (ADV). Droplets are composed of a volatile perfluorocarbon (PFC), such as perfluoropentane (PFP, 29 °C boiling point). A PFP emulsion does not spontaneously vaporize
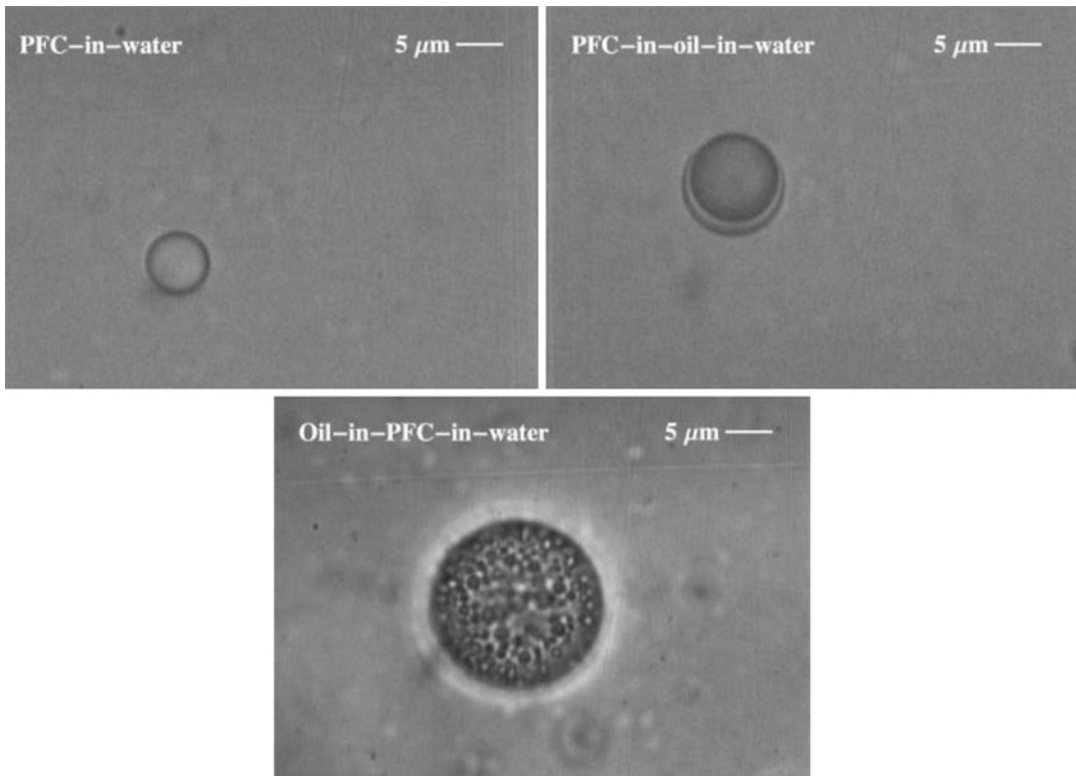
Fig. 9.1 PFC-in-water, PFC-in-oil-in-water and oil-in-PFC-in-water emulsions under the microscope

when injected *in-vivo* at 37 °C. However, upon exposure to ultrasound above certain acoustic pressure amplitudes, the PFP within the emulsion is vaporized. This opens up possibilities in a wide variety of diagnostic and therapeutic applications, such as embolotherapy (Zhang et al. 2010), aberration correction (Carneal et al. 2011) and drug delivery (Fabiilli et al. 2010a, b). Single and double emulsions of PFC-in-water and oil-in-PFC-in-water can be prepared, for instance, to encapsulate oil soluble drugs (Fig. 9.1).

PFC liquids are known for their use in medicine due to their biocompatibility and inertness (Biro et al. 1987). PFC nanodroplet emulsions can be utilized for selective extravasation in tumor regions (Long et al. 1978). Due to their biocompatibility and suggested ability to passively target regions of cancer growth, PFC droplets represent an attractive tool for cancer diagnosis. PFC droplets may also extravasate and be retained in the extravascular space due to the enhanced permeability and retention effect in

tumors (Rapoport et al. 2007; Zhang and Porter 2010). Extravasated droplets may be acoustically converted into gas bubbles allowing for ultrasound tumor imaging. At the same time PFC droplets are rich in fluorine, which makes them potential candidates as a contrast agent for MRI imaging. The availability of both intravascular contrast agents (microbubbles), and tumor-specific extravascular contrast agents (nanodroplets), would significantly increase diagnostic and therapeutic capabilities. Moreover, the droplets may be used to deliver chemotherapeutic agents to tumor regions, and locally release them upon exposure to triggered ultrasound (Rapoport et al. 2009).

9.2 Nonlinear Propagation

The amplitude of the acoustic pressure that is required to nucleate droplets in ADV turns out to be very high (Kripfgans et al. 2000). To obtain a

sufficiently high pressure, a focused ultrasound transducer is applied and the droplet is placed in the focal area of the emitted beam. Moreover, the frequency of the emitted ultrasound wave is several MHz. In a typical ADV experiment, the ultrasound wave travels a few centimeters (Kripfgans et al. 2000; Reznik et al. 2013; Shpak et al. 2013a, b; Giesecke and Hynynen 2003; Schad and Hynynen 2010; Williams et al. 2013) before impinging on the droplet. The high pressure, high frequency, applied focusing and long propagation distances are all factors that strengthen the nonlinear behavior of the ultrasound wave (Blackstock 1964; Bacon 1984). As a result, the wave that impinges on the droplet will be a highly deformed version of the one that is emitted by the transducer (Fig. 9.2). This has important consequences for the focusing inside the droplet, as will be demonstrated in Sect. 9.4.2.2.

9.2.1 Basic Equations for the Nonlinear Ultrasound Beam

Similar to most cases involving nonlinear medical ultrasound, the description of the beam that hits the droplet can be based on the Westervelt equation (Westervelt 1963; Hamilton and Morfey 2008):

$$\nabla^2 p - \frac{1}{c_0^2}\frac{\partial^2 p}{\partial t^2} + \frac{d}{c_0^4}\frac{\partial^3 p}{\partial t^3} = -\frac{b}{r_0 c_0^4}\frac{\partial^2 p^2}{\partial t^2} \tag{9.1}$$

where $\nabla^2 = \partial^2/\partial x^2 + \partial^2/\partial y^2 + \partial^2/\partial z^2$ is the Laplace operator and $p = p(x,y,z,t)$ denotes the acoustic pressure. The medium in which the ultrasound wave propagates is characterized by the ambient speed of sound c_0, the ambient density of mass ρ_0, the diffusivity of sound δ and
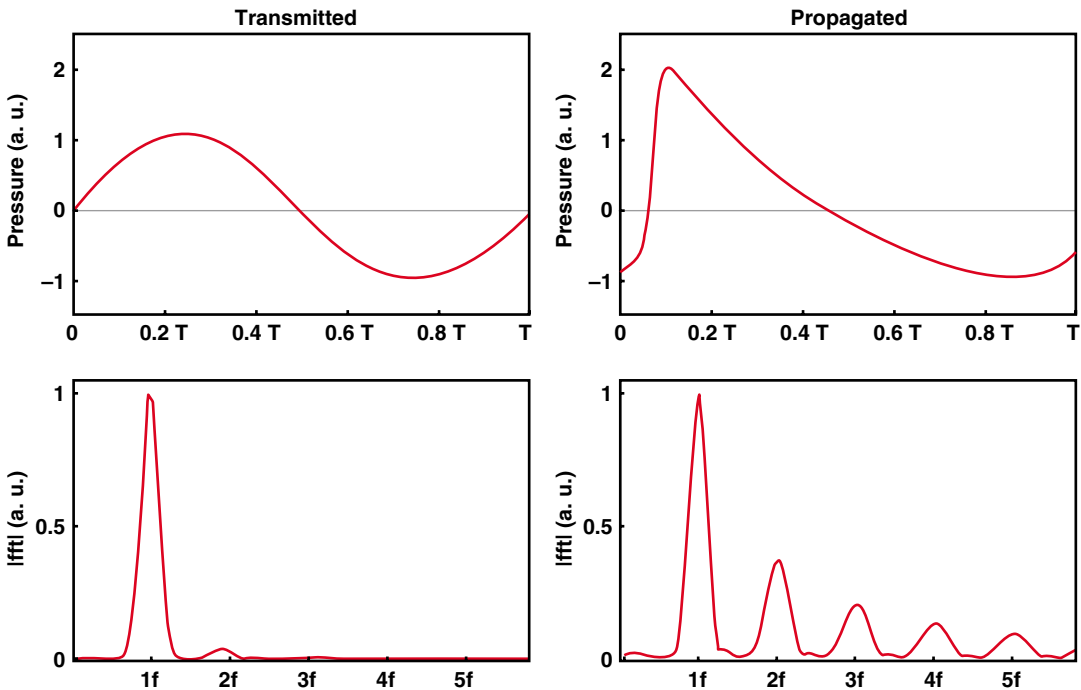

Fig. 9.2 Schematics of nonlinear propagation of an ultrasound wave. *T* and *f* are the period of oscillation and frequency of an ultrasound wave, respectively. Two upper plots are the transmitted and propagated wave, and two lower plots are their frequency domains. *–fft–* stands for the Fast Fourier Transform

the coefficient of nonlinearity β. Unfortunately, closed-form analytical solutions of this equation do not exist and its numerical solution generally requires considerable computational effort. However, in the present case of a narrow, focused beam and a homogeneous medium, some simplifying assumptions can be made. Firstly, it may be assumed that the predominant direction of propagation is along the transducer axis, which is taken in the z-direction. In this case, we can replace the ordinary time coordinate t by the retarded time coordinate $\tau = (t - t_0) - (z - z_0)/c_0$, which keeps the same value when traveling along with the wave. Here, t_0 is the time at which the transducer emits the pressure wave, and z_0 is the axial position of the transducer. The equivalent of Eq. 9.1 in the co-moving time frame is:

$$\nabla^2 \overline{p} - \frac{2}{c_0} \frac{\partial^2 \overline{p}}{\partial z \partial \tau} + \frac{\delta}{c_0^3} \frac{\partial^3 \overline{p}}{\partial \tau^3} = -\frac{\beta}{\rho_0 c_0^4} \frac{\partial^2 \overline{p}^2}{\partial \tau^2} \quad (9.2)$$

with $\overline{p} = \overline{p}(x, y, z, \tau)$ denoting the acoustic pressure in the co-moving time frame. Secondly, it may be assumed that in the retarded time frame the axial derivative $\partial^2 \overline{p}/\partial z^2$ is much smaller than the lateral derivatives $\partial^2 \overline{p}/\partial x^2$ and $\partial^2 \overline{p}/\partial y^2$. This motivates the use of the parabolic approximation $\nabla^2 \overline{p} \approx \nabla_\perp^2 \overline{p}$, where $\nabla_\perp^2 = \partial^2/\partial x^2 + \partial^2/\partial y^2$ is the Laplace operator in the lateral plane. This approximation is valid for waves propagating under at most 20° of the transducer axis (Lee and Pierce 1995). Applying the parabolic approximation to Eq. 9.2 and rearranging terms results in the Khokhlov-Zabolotskaya-Kuznetsov (KZK) equation (Zabolotskaya and Khokhlov 1969; Kuznetsov 1971):

$$\frac{\partial^2 \overline{p}}{\partial z \partial \tau} = \frac{c_0}{2} \nabla_\perp^2 \overline{p} + \frac{\delta}{2c_0^3} \frac{\partial^3 \overline{p}}{\partial \tau^3} + \frac{\beta}{2\rho_0 c_0^3} \frac{\partial^2 \overline{p}^2}{\partial \tau^2} \quad (9.3)$$

Dedicated coordinate transformations may be applied to improve the numerical solution in the far field (Hamilton et al. 1985; Hart and Hamilton 1988) or to adapt to specific forms of focused beams (Kamakura et al. 2000), but these will not be discussed here.

9.2.2 Numerical Solution for the Nonlinear Ultrasound Beam

We will follow a well-known numerical solution strategy (Lee and Hamilton 1995; Cleveland et al. 1996) that is based on the time integrated version of Eq. 9.3:

$$\frac{\partial \overline{p}}{\partial z} = \frac{c_0}{2} \int_{-\infty}^{\tau} \nabla_\perp^2 \overline{p}(\tau') d\tau' + \frac{\delta}{2c_0^3} \frac{\partial^2 \overline{p}}{\partial \tau^2} + \frac{\beta \overline{p}}{\rho_0 c_0^3} \frac{\partial \overline{p}}{\partial \tau}$$

$$(9.4)$$

The first term at the right-hand side of this equation accounts for the diffraction of the beam, the second term for its attenuation, and the third term for its nonlinear distortion. Further, the solution strategy is based on the split-step approach. This means that the field $\overline{p}$ is stepped forward over a succession of parallel planes with mutual distance Δz, where the field $\overline{p}(x, y, z_0, \tau)$ in the transducer plane acts as the starting plane. The stepsize Δz is taken sufficiently small, allowing that each of the above phenomena may be accounted for in separate sub steps (Varslot and Taraldsen 2005). Therefore, the total step $z \rightarrow z + \Delta z$ involves the numerical solution of the separate equations:

$$\frac{\partial \overline{p}}{\partial z} = \frac{c_0}{2} \int_{-\infty}^{\tau} \nabla_\perp^2 \overline{p}(\tau') d\tau' \quad (9.5)$$

$$\frac{\partial \overline{p}}{\partial z} = \frac{\delta}{2c_0^3} \frac{\partial^2 \overline{p}}{\partial \tau^2} \quad (9.6)$$

$$\frac{\partial \overline{p}}{\partial z} = \frac{\beta \overline{p}}{\rho_0 c_0^3} \frac{\partial \overline{p}}{\partial \tau} \quad (9.7)$$

over the same interval, where the result of solving one equation is used as the input for solving the next one. A numerical implementation of the above process is used to step the acoustic pressure from the transducer to the focus of the beam, i.e. the location of the droplet. For convenience, it is now assumed that the droplet is located at the origin of the coordinate system and that the source emits the pressure wave at $t_0 = z_0/c_0$. This

makes $\tau = t$ at the position of the droplet. For ease of notation, the bar and the coordinates of the droplet will be suppressed, and the pressure at the droplet position, as obtained from the numerical solution of the KZK-equation, will simply be indicated by $p_{KZK}(t)$.

9.2.3 Nonlinear Pressure Field at the Focus of the Beam

The nonlinear pressure field at the focus of the beam can be expanded in a Fourier series:

$$p_{KZK}(t) = \sum_{n=0}^{\infty} a_n \cos(n\omega t + \phi_n)$$
$$= \mathrm{Re}\left[\sum_{n=0}^{\infty} a_n e^{i(n\omega t + \phi_n)}\right] \quad (9.8)$$

where a_n and ϕ_n are the amplitudes and the phases of the $n-th$ harmonic component of the ultrasound wave. For convenience, all the subsequent derivations will be given in the complex representation, so we will omit taking the real part and simply write:

$$p_{KZK}(t) = \sum_{n=0}^{\infty} a_n e^{i(n\omega t + \phi_n)} \quad (9.9)$$

Given that nonlinear deformation of the waveform builds up over distance and the droplet is four orders of magnitude smaller in size than the distance to the transducer, the additional nonlinear distortion inside the droplet is neglected. This implies that wave propagation inside the droplet is considered linear, so the superposition theorem holds, and the focusing of each harmonic component in the droplet may be analyzed on an individual basis, as will be done in Sect. 9.4.2.2.

9.3 Bubble Dynamics

9.3.1 Dynamics of a Gas Bubble

Bubble radial oscillations are governed by the Rayleigh-Plesset equation:

$$\ddot{R}R + \frac{3}{2}\dot{R}^2 = \frac{\Delta P}{\rho} \quad (9.10)$$

where R, $\dot{R}$, and $\ddot{R}$ are the radius, the velocity and the acceleration of the bubble wall, respectively, and ρ is the density of the liquid. $\Delta P = P_L(R) - P_\infty$ is the pressure difference between the liquid at the bubble wall $P_L(R)$ and the external pressure infinitely far from the bubble p_∞. Equation 9.10 was first described by Lord Rayleigh (1917) for the case $\Delta P = 0$ and was later refined (Plesset 1949; Noltingk and Neppiras 1950; Neppiras and Noltingk 1951; Poritsky 1952). It is derived for a spherically symmetric bubble, and follows from the Bernoulli's equation and the continuity equation (Leighton 1994). Equation 9.10 assumes spherical symmetry of the bubble, and the motion of the liquid around the bubbles is considered to be spherically symmetric. The liquid is incompressible.

The bubble is assumed to be much smaller than the acoustic wavelength, such that acoustic pressure is considered to be uniform. Thus, the pressure at infinity is the sum of the acoustic forcing $P(t)$ and the ambient pressure P_0:

$$p_\infty = P(t) + P_0 \quad (9.11)$$

The interfacial pressure acting on the liquid at the bubble wall consists of the Laplace pressure $2\sigma/R_0$, viscous pressure $4\mu\dot{R}/R$ and the gas pressure P_g. Neglecting the vapor pressure of the liquid, the gas pressure inside the bubble as a function of the bubble radius R can be described by the ideal gas relation $P_g V^\gamma = const$, where γ is the polytropic constant and $V \propto R^3$ is the bubble volume. For this derivation we first neglect the gas diffusion. Thus, the total number of gas molecules inside the bubble is constant. In equilibrium, the pressure inside the bubble P_{eq} is equal to the sum of the ambient pressure P_0 and the Laplace pressure:

$$P_{eq} = P_0 + \frac{2\sigma}{R_0} \quad (9.12)$$

where σ and R_0 are the surface tension and the equilibrium radius, respectively. In combination with the ideal gas law, the dependence of the gas pressure as a function of the bubble radius can be

written as $P_g = \left(P_0 + \dfrac{2\sigma}{R_0} \right)\left(\dfrac{R_0}{R} \right)^{3\gamma}$. The right-hand side of Eq. 9.10 can then be written as:

$$\Delta P = \left(P_0 + \frac{2\sigma}{R_0} \right)\left(\frac{R_0}{R} \right)^{3\gamma} - P_0 - \frac{2\sigma}{R}$$
$$-4\mu \frac{\dot{R}}{R} - P(t) \quad (9.13)$$

which gives the final form of the bubble dynamic equation:

$$\rho\left(\ddot{R}R + \frac{3}{2}\dot{R}^2 \right) = \left(P_0 + \frac{2\sigma}{R_0} \right)\left(\frac{R_0}{R} \right)^{3\gamma}$$
$$-P_0 - \frac{2\sigma}{R} - 4\mu \frac{\dot{R}}{R} - P(t) \quad (9.14)$$

The microbubbles in the ultrasound contrast agents can be encapsulated with a phospholipid, protein or polymer coating, thus preventing bubbles from dissolution. For more details please see (Marmottant et al. 2005; de Jong et al. 2007; Church 1995). The viscoelastic coating also contributes to an increased stiffness and to additional viscous damping (Overvelde et al. 2010).

9.3.2 Linearization

The acoustic pressure typically has the form of a sinusoidal oscillation $P(t) = P_A \sin(\omega t)$, with P_A being the driving pressure amplitude, and ω the driving pressure angular frequency. With relatively small oscillation amplitudes Eq. 9.10 can be linearized. To rewrite Eq. 9.10 in linear terms we express the bubble radius R as:

$$R = R_0 (1 + x) \quad (9.15)$$

with R_0 the equilibrium radius, as before, and $x \ll 1$ a small dimensionless perturbation to the radius. Substituting Eq. 9.15 into Eq. 9.10 and retaining only first-order terms, x, $\dot{x}$ and $\ddot{x}$ gives:

$$\ddot{x} + 2\beta\dot{x} + \omega_0^2 x = \frac{P_A}{\rho R_0^2}\sin(\omega t) \quad (9.16)$$

where

$$\omega_0 = \sqrt{\frac{1}{\rho R_0^2}\left[3\gamma\left(P_0 + \frac{2\sigma}{R_0} \right) - \frac{2\sigma}{R_0} \right]} \quad (9.17)$$

the eigenfrequency of bubble oscillations, and:

$$\beta = \frac{2\mu}{\rho R_0^2} \quad (9.18)$$

the damping due to viscosity. The damping has the dimensions of the reversed time $\left[s^{-1} \right]$ and represents how fast the amplitude of oscillations is decaying in time due to the energy loss.

The solution to the equation Eq. 9.16 is:

$$x(t) = X_t e^{-\beta t}\cos(\omega_1 t) + X_s \cos(\omega t + \phi_1) \quad (9.19)$$

with the ϕ_1 being the phase shift between the two terms:

$$\phi_1 = \arctan\left(\frac{\omega_0^2 - \omega^2}{2\beta\omega} \right) \quad (9.20)$$

The first term of Eq. 9.19 is the transient solution. Its amplitude dampens out in time as $X_t e^{-\beta t}$, where X_t is the amplitude of transient oscillations at time $t_0 = 0$. Not only the viscosity of water can contribute to the damping, but also the acoustic reradiation and the viscosity of the coating shell and thermal damping. For more details please see (Overvelde et al. 2010). The frequency of the transient solution is equal to $\omega_1 = \sqrt{\omega_0^2 - \beta^2}$. The amplitude of the transient solution X_t depends strongly on the initial conditions.

The second term of Eq. 9.19 is the steady-state solution. The amplitude of the steady-state response depends on the driving frequency as:

$$X_s = \frac{P_A}{\rho R_0^2}\frac{1}{\sqrt{\left(\omega_0^2 - \omega^2 \right)^2 + 4\omega^2\beta^2}} \quad (9.21)$$

The resonance frequency ω_{res} of the system, by definition, corresponds to the maximal amplitude of the steady-state solution. X_s is at maximum, when the denominator in the Eq. 9.21 is at minimum. Thus, the resonance frequency relates to the eigenfrequency ω_0 as:

$$\omega_{\text{res}} = \sqrt{\omega_0^2 - 2\beta^2} \quad (9.22)$$

The smaller the damping β, the closer the resonance frequency to the eigenfrequency of the bubble oscillations. Additionally, for large bubbles, when the Laplace pressure is small compared to the ambient pressure Eq. 9.17 simplifies to:

$$\omega_M = 2\pi f_M = \sqrt{3\gamma \frac{P_0}{\rho R_0^2}} \qquad (9.23)$$

with f_M the Minnaert eigenfrequency, resonance frequency of the bubble (Minnaert 1933). Relation Eq. 9.23 tells us that the resonance frequency can be estimated directly from the bubble radius R_0. For a bubble in water at standard pressure ($P_0 = 100 \text{kPa}$, $\rho = 1000 \text{kg/m}^3$), the equation becomes $f_M R_0 \approx 3.26 \, \mu\text{m.MHz}$. The smaller the bubble radius, the higher the resonance frequency becomes.

It is insightful to make the analogy to the classical mass-spring system. The dynamics of the classical mass spring system is governed by the equation:

$$\ddot{x} + 2\frac{\beta'}{m}\dot{x} + \omega_0'^2 x = \frac{F_0}{m}\sin(\omega t) \qquad (9.24)$$

where $\omega'_0 = \sqrt{k/m}$ is the eigenfrequency, β' is the damping constant, k is the spring stiffness, F_0 is the driving force and m is the mass. Equation 9.24 has the same form as Eq. 9.16. Thus, a gas inside the bubble, represented by the polytropic constant γ, acts as the restoring force, the liquid around the bubble acts as a mass $\left(4\pi R_0^3 \rho\right)$, and ultrasound is acting as a driving force $\left(12\pi\gamma R_0 P_0\right)$.

9.3.3 Pressure Emitted by the Bubble

Far from the bubble wall, at a distance r, the velocity of the liquid v_r can be calculated from the continuity equation (Prosperetti 2011):

$$4\pi r^2 v_r = 4\pi R^2 \dot{R} \qquad (9.25)$$

$$v_r = \frac{R^2}{r^2}\dot{R} \qquad (9.26)$$

The liquid is incompressible and the bubble wall and the liquid motion around the bubble are spherically symmetric. $\dot{R}$ is the velocity of the bubble wall in the radial direction, as before.

The pressure field, generated by the radial bubble wall oscillations, can be calculated from the Euler equation (Prosperetti 2011):

$$\rho\frac{\partial v}{\partial t} + \frac{\partial p}{\partial r} = 0 \qquad (9.27)$$

where p is the pressure emitted by the bubble. In Eq. 9.27 we omit the nonlinear convective term. Substituting the expression of the velocity field (Eq. 9.26) into Eq. 9.27 gives the pressure gradient:

$$\frac{\partial p}{\partial r} = -\frac{\rho}{r^2}\frac{d}{dt}\left(R^2\dot{R}\right) \qquad (9.28)$$

and the pressure emitted by the bubble:

$$p = \frac{\rho}{r}\frac{d}{dt}\left(R^2\dot{R}\right) = \rho\left(\frac{R^2\ddot{R} + 2R\dot{R}^2}{r}\right) \qquad (9.29)$$

9.3.4 Secondary Bjerknes Force

Let us now consider two interacting gas bubbles, separated by a distance l. The distance between the bubbles 1 and 2 is much larger that their radii $R_1(t)$ and $R_2(t)$. Thus, we can consider the motion of the liquid around the bubbles to be spherically symmetric. Bubble 2 with volume $V_2 = \frac{4}{3}\pi R_2^3$ experiences a force F_{12} as a result of the pressure emitted by bubble 1, p_1 (Leighton 1994):

$$F_{12} = -V_2 \nabla p_1 \qquad (9.30)$$

The force is directed along the line, which connects the centers of the two interacting bubbles. Substitution of Eq. 9.28 (expression for the pressure gradient generated by the first bubble) into Eq. 9.30 yields the force of the first bubble on the second one at a distance l:

$$F_{12} = -V_2 \left.\frac{\partial p_1}{\partial r}\right|_{r=l} = V_2 \frac{\rho}{l^2} \frac{d}{dt}\left(R_1^2 \dot{R}_1\right)$$

$$= \frac{\rho}{4\pi l^2} V_2 \frac{d^2 V_1}{dt^2} \qquad (9.31)$$

where $V_1 = \frac{4}{3}\pi R_1^3$ the volume of bubble 1.

The net radiation force acting on a neighboring bubble is called the secondary Bjerknes force F_B after Bjerknes (Bjerknes 1906). The time averaged equation $\langle F_{12}\rangle$ is obtained by integrating Eq. 9.31 over the period of volume oscillations by partial integration:

$$F_B = \langle F_{12}\rangle = -\frac{\rho}{4\pi d^2}\langle \dot{V}_1 \dot{V}_2\rangle \qquad (9.32)$$

A positive value of $\langle \dot{V}_1 \dot{V}_2\rangle$ corresponds to attraction of the bubbles, and a negative value to repulsion. This means that the bubbles that oscillate with the same phase will attract each other. Note also the symmetry of Eq. 9.32. To calculate the force of the second bubble on the first one $\langle F_{21}\rangle$, one just needs to exchange indexes $1 \leftrightarrow 2$. $\langle F_{21}\rangle$ has the same magnitude, but an opposite direction as $\langle F_{12}\rangle$.

9.4   Droplet Dynamics

9.4.1   Oscillatory Translations

The typical pressure amplitudes, which are used to activate perfluorocarbon droplets, are two orders of magnitude higher that those used to drive ultrasound contrast agents. Water itself always experiences periodic compression as a result of ultrasound forcing (Leighton 1994). Let us express such oscillations as:

$$\epsilon = \epsilon_0 \sin\left(\omega t - kx\right) \qquad (9.33)$$

where ϵ is the fluid particle displacement. The acoustic impedance, by definition, is the ratio of the driving pressure to the fluid particle velocity (Leighton 1994):

$$Z = P_A / \dot{\epsilon}_0 \qquad (9.34)$$

where $\dot{\epsilon}_0$ is the particle displacement velocity amplitude, and P_A is the acoustic pressure amplitude. The $\dot{\epsilon}_0$ particle velocity amplitude relates to the particle displacement amplitude ϵ_0 as $\dot{\epsilon}_0 = \omega\epsilon_0$, which follows from Eq. 9.33 by taking its time derivative. The dP pressure change with respect to the equilibrium value is related to a dV volume change by the bulk modulus B, defined by (Leighton 1994):

$$dP = -B\frac{dV}{V} \qquad (9.35)$$

Equation 9.35 can be used to calculate the acoustic pressure P at any given spatial point x_0 as $P(x_0) = -B\left.\frac{\partial \epsilon}{\partial x}\right|_{x=x_0}$. Applying this relation to Eq. 9.33 gives $P_A = Bk\epsilon_0$, or $P_A = B\frac{k}{\omega}\dot{\epsilon}_0$. The acoustic impedance Eq. 9.34 can then be written as:

$$Z = B\frac{k}{\omega} \qquad (9.36)$$

or by using the equation for the wave speed $c = \omega / k = \sqrt{B/\rho}$:

$$Z = \rho c \qquad (9.37)$$

With the relations given above, one can now estimate the oscillatory translational amplitude. For the case of $f = 3.5\text{MHz}$, $P_A = 8\text{MPa}$ and $c_\omega = 1522\text{m/s}$, the speed of sound in water at 37 °C, the amplitude is $\epsilon_0 = P_A / 2\pi\rho f c_\omega = 210\text{nm}$.

The acoustic impedance $Z = \rho c$ has the analogy with a refractive index n in optics. The ultrasound wave at the interface of two substances with different acoustic impedances Z_1 and Z_2 will experience a reflection and a refraction, similarly as light would experience at the interface with two different refractive indexes n_1 and n_1.

Let us now denote θ_I, θ_R, and θ_T the incident, the translated and the reflected angles, respectively (Fig. 9.3). One can derive the relation between these angles by considering continuity of the normal displacement at the interface.

Fig. 9.3 Schematics of reflection and transmission of a wave of displacement
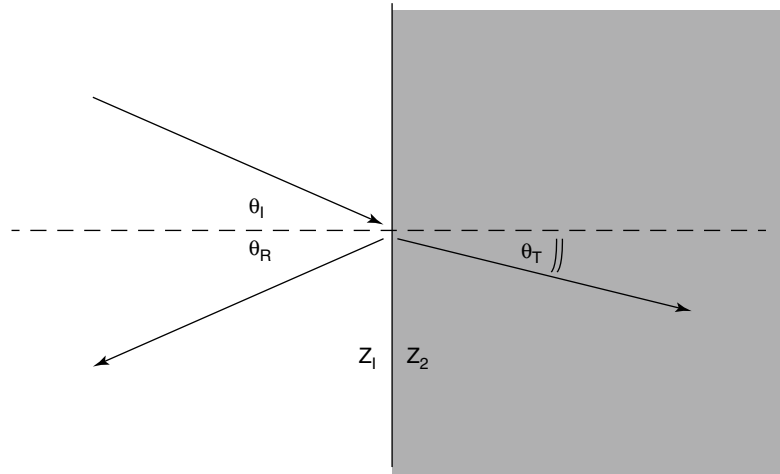
This gives Snell's reflection law $\sin(\theta_I) = \sin\theta_R$ and $c_2 \sin\theta_I = c_1 \sin\theta_T$, where c_1 and c_2 are the speed of sound of the first and the second medium, respectively (Leighton 1994).

9.4.2 Focusing inside a Spherical Droplet

When an interface between two acoustic media has a finite curvature R, as in the case of a spherical droplet, acoustic focusing is observed. This is a similar effect as the focusing of light by an optical lens. First, the case of large droplets is considered, i.e. when the acoustic wavelength λ is much smaller than the droplet radius R. Next, the case where λ is of the order of R, or even larger, is considered.

9.4.2.1 Case 1: Droplets much Larger in Size than the Wavelength

When $\lambda \ll R$, the refraction formulas provided by the theory of geometrical scattering apply. When a parallel beam of light travels in a medium with refractive index n_1 and encounters a spherical interface between this medium and a second medium with refractive index n_2, either the transmitted or the reflected wave focuses in a point at a distance:

$$f = R\frac{n_2}{n_2 - n_1} \tag{9.38}$$

This distance is measured from the intersection point of the interface and the beam axis, which crosses the center of the curvature (Fig. 9.4).

In analogy with the optical focus, an acoustic focus can be calculated for the case $\lambda \ll R$ by simply replacing n_1 / n_2 with c_1 / c_2 in the equation above. This gives:

$$f = R\frac{c_1}{c_1 - c_2} \tag{9.39}$$

For instance, when a large spherical perfluoropentane droplet with $c_2 = 406\,\text{m/s}$ is immersed in water with $c_1 = 1522\,\text{m/s}$ (at 37 °C), the acoustic focus is at $f = 1.36R$. This means that the acoustic wave focuses on a distal side, $0.36R$ away from the geometrical droplet center.

9.4.2.2 Case 2: Droplets Similar or Smaller in Size than the Wavelength

The situation complicates when the radius of the droplet is of the same order of magnitude as the wavelength, or even smaller, i.e. when $\lambda \sim R$ or $\lambda \gg R$. Experimental data obtained with small droplets shows that the ultrasound beam focuses on the proximal side of the droplet, which is not in agreement with the prediction above. Obviously, in this case geometrical considerations can no longer be applied, and a full wave theory must be applied. Figure 9.5 shows the configuration of the acoustic

Fig. 9.4 Schematics of the focusing of an acoustic wave on the droplet sphere when the acoustic wavelength is much larger than the droplet radius
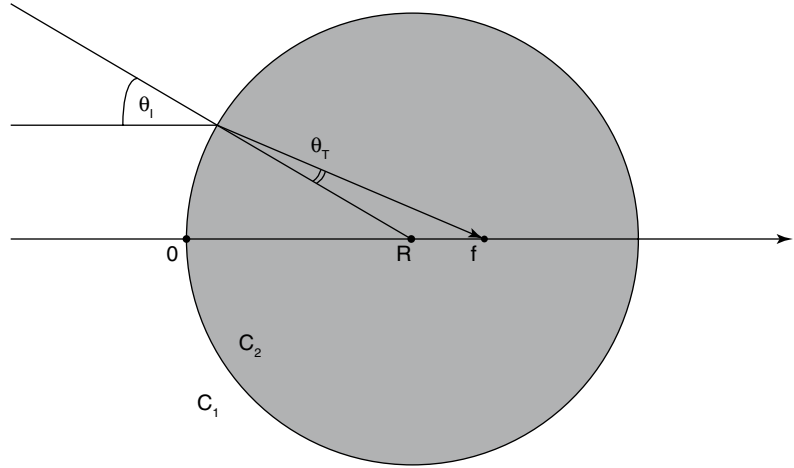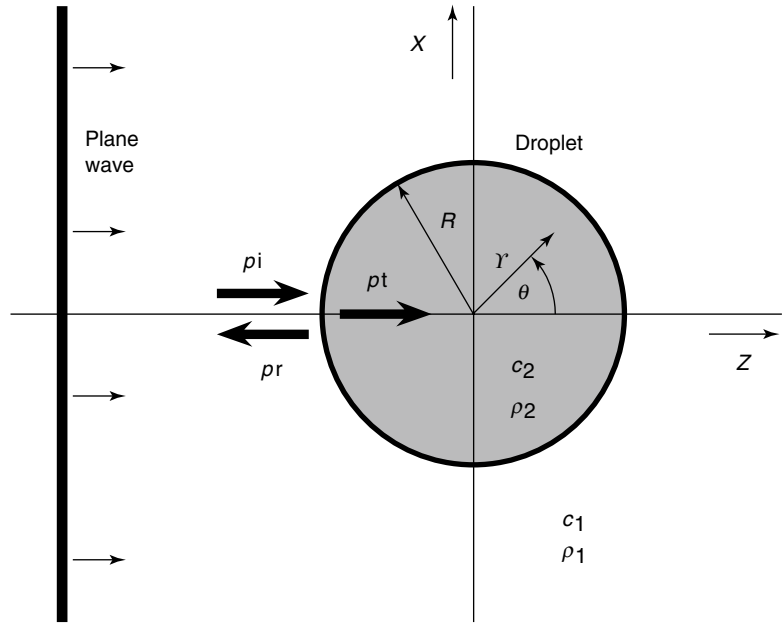

Fig. 9.5 Configuration of the droplet and the incident, transmitted, reflected ultrasound waves

diffraction problem that will be solved here. Throughout the derivations, the parameters of the surrounding medium are labeled with a subscript 1, and the parameters of the medium inside the droplet are labeled with a subscript 2.

At the location of the droplet, the incident ultrasound wave is considered to be planar. In view of Eq. 9.9, it is written as:

$$p_i\left(x,y,z,t\right)=\sum_{n=0}^{\infty}a_n e^{i\left(n\omega t-nk_1 z+\phi_n\right)} \quad (9.40)$$

where $k_1=\omega/c_1$ is the wave number outside the droplet. To keep the derivations simple, the

diffraction problem will first be solved for one spectral component:

$$p_i\left(x,y,z,t\right)=ae^{i\left(\omega t-k_1 z+\phi\right)} \quad (9.41)$$

In view of the spherical symmetry of the configuration, it is convenient to apply a coordinate transformation from cartesian coordinates (x,y,z) to spherical coordinates (r,θ,ϕ), where ϕ is the azimuthal angle measured with respect to the positive z-axis, and ϕ is the elevation angle in the xy-plane. Due to the waves having rotational symmetry with respect to the z-axis, there will be no dependence on ϕ, and this coordinate will be omitted. In spherical coordinates,

the incident pressure wave can be written as a summation of spherical harmonics:

$$p_i(r, \theta, t) = ae^{i(\omega t + \phi)} \sum_{m=0}^{\infty} \gamma_m j_m(k_1 r) P_m(\cos\theta)$$

$$(9.42)$$

Here, $\gamma_m = (2m+1)(-i)^m$, j_m is the spherical Bessel function of the first kind and order m, and P_m is the $m-$th order Legendre polynomial. The spherical Bessel function j_m is related to the ordinary Bessel function J_m according to $j_m(x) = \sqrt{(\pi/2x)} J_{m+1/2}(x)$.

When the incident wave encounters the droplet, it gives rise to a transmitted wave inside the droplet:

$$p_t(r, \theta, t) = ae^{i(\omega t + \phi)} \alpha_m j_m(k_2 r) P_m(\cos\theta)$$

$$(9.43)$$

and a reflected wave outside the droplet:

$$p_r(r, \theta, t) = ae^{i(\omega t + \phi)} \beta_m h_m^{(2)}(k_1 r) P_m(\cos\theta)$$

$$(9.44)$$

In these equations, $k_2 = \omega / c_2$ is the wave number inside the droplet, and $h_m^{(2)}$ is the spherical Hankel function of the second kind and order m. The spherical Hankel function $h_m^{(2)}$ is related to the ordinary Hankel function $H_m^{(2)}$ following $h_m^{(2)}(x) = \sqrt{(\pi/2x)} H_{m+1/2}^{(2)}(x)$. At the spherical interface between the outside and the inside of the droplet, the pressure and the radial particle velocity should be continuous. The latter requirement can be translated into a condition on the radial derivative of the pressure. In mathematical form, the boundary conditions at the interface are:

$$\lim_{r\downarrow R}\left[p_i(r,\theta,t) + p_r(r,\theta,t)\right] = \lim_{r\uparrow R} p_t(r,\theta,t)$$

$$(9.45)$$

$$\lim_{r\downarrow R}\frac{1}{\rho_1}\frac{\partial}{\partial r}\left[p_i(r,\theta,t) + p_r(r,\theta,t)\right]$$
$$= \lim_{r\uparrow R}\frac{1}{\rho_2}\frac{\partial}{\partial r}p_t(r,\theta,t)$$

$$(9.46)$$

which should hold for all θ and t. Substitution of Eqs. 9.42, 9.43, and 9.44 into these boundary conditions results in a system of two equations for α_m and β_m. Solution of this system yields:

$$\alpha_m = \gamma_m \frac{Z_2 j_m(k_1 R) h_m^{(2)\prime}(k_1 R) - Z_2 h_m^{(2)}(k_1 R) j'_m(k_1 R)}{Z_2 j_m(k_2 R) h_m^{(2)\prime}(k_1 R) - Z_1 h_m^{(2)}(k_1 R) j'_m(k_2 R)}$$

$$(9.47)$$

$$\beta_m = \gamma_m \frac{Z_1 j_m(k_1 R) j'_m(k_2 R) - Z_2 j_m(k_2 R) j'_m(k_1 R)}{Z_2 j_m(k_2 R) h_m^{(2)\prime}(k_1 R) - Z_1 h_m^{(2)}(k_1 R) j'_m(k_2 R)}$$

$$(9.48)$$

where $Z_1 = \rho_1 c_1$ and $Z_2 = \rho_2 c_2$ are the acoustic impedances of the media outside and inside the droplet, respectively. The prime indicates the derivative of a function. The constant α_m can be considered as the transmission coefficient of the droplet interface for spherical harmonics of order m, and the constant β_m can be considered as the corresponding reflection coefficient. At this stage, the problem of finding the wave inside the droplet due to a single sinusoidal component of the incident wave is solved.

To find the wave that is formed inside the droplet by the nonlinear incident wave, all the transmitted waves caused by the individual components of the incident wave must be added. The result is:

$$p_{inside}(r, \theta, t) = p_t(r, \theta, t) = \sum_{n=0}^{\infty}\sum_{m=0}^{\infty} a_n e^{i(n\omega t + \phi_n)} \alpha_{n,m} j_m(nk_1 r) P_m(\cos\theta)$$

$$(9.49)$$

where $\alpha_{m,n}$ follows from Eq. 9.47 by replacing k_1 by nk_1 and k_2 by nk_2. This equation can be used to calculate the pressure in any position (r, θ, φ) at any time t. Numerical implementation

requires that both summations involve a finite number of terms. This forms no significant limitation, because in practice only a limited number of N harmonics will give a significant contribution to the ultrasound field inside the droplet, and only a limited number of M spherical harmonics is required to accurately represent this field. However, another numerical issue arises when the radius of the droplet is much smaller than the wavelength. In this case, the numerical results for the spherical Bessel and Hankel functions may contain large errors. This problem may be eliminated by first approximating these functions by their series expansion around zero. With the full pressure field determined both in space and time we can now find the local maximum of pressure - the focus.

The pressure amplification factor in the focusing spot, as well as its location, depend on the input parameter values, i.e. the pressure amplitude, the frequency and the transducer geometry and size, which prescribe the focusing strength and the propagation distance to the focal point. For instance, in case of a $R = 10\,\mu m$ perfluoropentane droplet immersed in water and insonified with an incoming ultrasound wave with a peak negative pressure $P_i^- = -4.5\,MPa$ and frequency $f = 3.5\,MHz$ ($\lambda = 430\,\mu m$ in water at 37 °C) coming from a transducer with a 3.81 cm focal distance, a focused peak negative pressure of $P_{inside}^- = -26\,MPa$ is achieved within the droplet (Fig. 9.6). Thus, a near six-fold increase in the peak negative pressure amplitude is observed in a concentrated region on the proximal side around $z = -0.4R$.

From Eq. 9.47 it follows that the pressure inside the droplet, due to a single incident wave component, depends on the dimensionless product ωR. When for two droplets with different radii R_1 and R_2 the relation $\omega_1 R_1 = \omega_2 R_2$ holds, an incident wave with frequency f_1 encountering a droplet with radius R_1 is focused at the same relative position within the droplet as an incident wave with frequency f_2 that hits a droplet with radius R_2. This implies that when larger droplets turn out to vaporize more easily than smaller droplets at the same frequency, it also follows that for the same radius droplets are easier to evaporate at high
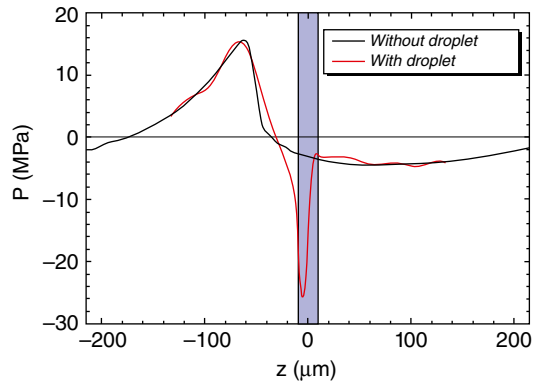

Fig. 9.6 Schematics of the superharmonic focusing effect within a perfluoropentane spherical droplet. The *black line* represents the acoustic pressure waveform on the axis of symmetry ($\theta = 0$) as a function of the z-coordinate in the absence of a droplet. The *red solid line* is the focused pressure in presence of the droplet. The snapshot represents the moment of minimum focused pressure both in time and space. The *blue shaded* region depicts the position of the droplet

frequencies than at low frequencies, and vice-versa.

However, nonlinear propagation makes this picture more complex. First, the higher the acoustic pressure amplitude, the more nonlinear the wave becomes as the amplitudes of the higher harmonics build up roughly as $\left(P_{surface}\right)^{n-1}$, where $P_{surface}$ is the pressure amplitude at the transducer surface and n is the number of the particular harmonic. Second, the nonlinear propagation depends on the frequency. Additionally, of course, the nonlinear beam is focused differently from the linear one, with different pressure amplification factors and focusing positions for each harmonic. Finally, the shape of the nonlinearly distorted wave is strongly dependent on the parameters of the propagating media. For human tissue the Goldberg ratio is lower than for water (Szabo et al. 1999). This indicates that nonlinear distortion is easier to achieve in water compared to tissue. Therefore the experiments performed *in-vivo* are expected to have different nucleation patterns, with a higher nucleation threshold compared to the *in-vitro* experiments.

Knowledge of the physics of acoustic focusing in small droplets is important for the optimization of acoustic droplet vaporization for therapeutic applications. This is particularly the

case for attaining activation at low acoustic pressures, thereby minimizing the negative bio-effects associated with the use of high-intensity ultrasound. Moreover, it helps in the design of droplets: by mixing liquids with different physical properties, the acoustic impedance may be tuned through a change of the density of mass and/or the speed of sound. Using dedicated waveforms, the amplitudes and phases of the nonlinear wave at the focus of the beam can be optimized to obtain maximal constructive interference within the droplets and obtain maximal focusing strength at any particular acoustic input pressure. Moreover, the knowledge of consecutive droplet vaporization dynamics is important because it affects the surrounding tissue and may cause damage. It is not only the acoustic impedance mismatch between the droplet and the surrounding media that determines the interior pressure, but also the exterior of the droplet. Here we have only considered single droplets, but clouds of droplets may cause complicated pressure scattering patterns and may lead to different focusing spots. One can also think of periodic arrangements of monodisperse droplets to observe similar diffraction relations as we have with light passing through crystals.

9.4.3 Radial Vapor Bubble Expansion

There are three main physical mechanisms that govern the vapor bubble growth process: phase-change, heat transfer and inertia. There are also two phenomena, which can limit vapor bubble growth. Firstly, the vapor bubble pushes the surrounding liquid as it grows. The force by which the liquid is pushed is determined by the pressure which acts on the bubble wall. The surrounding liquid has inertia, and the vapor bubble growth rate will be limited by this inertia. Secondly, the phase-change from liquid to vapor is an endo-thermic process, requiring heat absorption. The required heat for vaporization is transferred from the liquid around the bubble by cooling the surroundings. The rate of this process is limited by heat transfer.

Let us now first have a closer look at inertial growth limitation. Here we assume that the heat transfer is high enough to supply the required energy for the endothermic phase-transition. In this case the Rayleigh-Plesset equation can be written as:

$$\ddot{R}R + \frac{3}{2}\dot{R}^2 = \frac{P_v - P_\infty}{\rho} \qquad (9.50)$$

where P_v is the vapor pressure and P_∞ is the pressure far away from the bubble wall. We disregard the surface tension, the sound reradiation and the viscosity. The boiling temperature of the liquid is T_b and the ambient temperature is T_∞. The liquid is superheated ($T_\infty > T_b$) so that $P_v > P_\infty$. The vapor pressure P_v is a function of the temperature and assumed to be constant during vapor bubble growth. Initially the velocity of the bubble wall $\dot{R}$ is small, and the first term on the left hand side of Eq. 9.50 is dominant. After approximately a few nanoseconds at $P_v = 1.4P_\infty$, the bubble wall velocity reaches its terminal value and the second term on the right hand side of Eq. 9.50 becomes dominant.

Terminal velocity is reached at the condition $\ddot{R} \to 0$. Substituting this into Eq. 9.50 and integrating with the initial condition $R(t = 0) = 0$ gives the radius-time dependency of the inertially limited vapor bubble growth:

$$R(t) = \left(\frac{2}{3}\frac{(P_v - P_\infty)}{\rho}\right)^{1/2} t \qquad (9.51)$$

Equation 9.51 is linear with time and is faster for higher vapor pressures P_v, thus at higher ambient temperatures T_∞.

Let us now have a look at the second case, where we focus on heat transfer and where inertial limitations are neglected. Contrary to the solution of the inertial problem, the heat transfer is complicated by the temperature distribution outside the vapor bubble (Fig. 9.7).
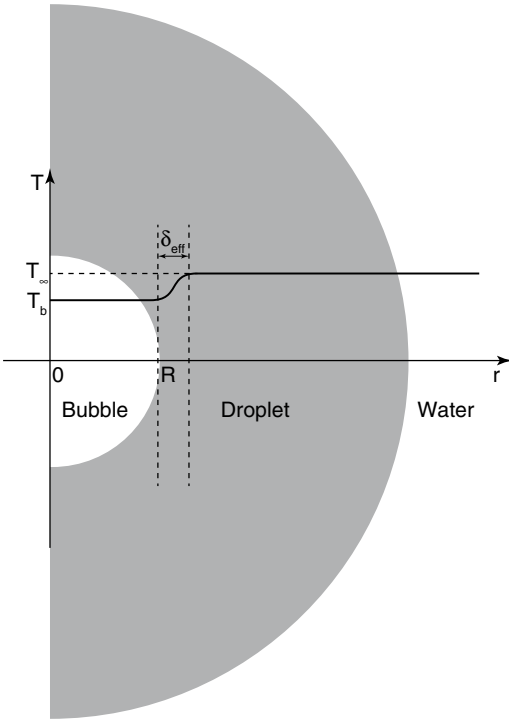
Fig. 9.7 Schematics of temperature distribution during the vaporization of a superheated perfluorocarbon droplet immersed in water. T_b is boiling temperature of perfluorocarbon, T_∞ is ambient temperature and δ_{eff} is effective thermal boundary layer around the vapor bubble of the radius R

The temperature distribution changes with time due to thermal diffusion. In addition, it is also affected by the expansion of the bubble, as described by the continuity equation. The effective thermal boundary layer around the vapor bubble is determined by (Prosperetti 2011):

$$\delta_{eff} = \sqrt{Dt} \qquad (9.52)$$

where D is the thermal diffusivity of the liquid. This estimation follows from the thermal diffusion equation and shows that the thermal boundary layer diffuses with time as $\sqrt{t}$. On the vapor side of the thermal boundary layer the temperature is T_b, and on the liquid side of the thermal boundary layer the temperature is T_∞. The effective temperature gradient over the thermal boundary layer is $\Delta T / \delta_{eff}$, where $\Delta T = T_\infty - T_b$ is the temperature difference. The heat flow W_1 inside the vapor bubble from the surrounding liquid caused by the temperature mismatch can be estimated as follows:

$$W_1 = 4\pi R^2 k \frac{\Delta T}{\sqrt{Dt}} \qquad (9.53)$$

where k is the heat transfer coefficient and $4\pi R^2$ is the interfacial area.

The latent heat energy per unit time W_2 required to supply the vapor bubble growth is:

$$W_2 = 4\pi R^2 L \rho_v \frac{dR}{dt} \qquad (9.54)$$

with L the latent heat, and $4\pi R^2 \rho_v \frac{dR}{dt}$ the derivative of the mass, with ρ_v the density of the vapor. Equalizing Eqs. 9.53 and 9.54, and integrating with the initial condition $R(t=0)=0$, gives the radial dynamics of the heat transfer limited vapor bubble growth:

$$R(t) = 2\frac{k\Delta T}{L\rho_v \sqrt{D}}\sqrt{t} \qquad (9.55)$$

It is dependent on time t following a square root behavior, and eventually will become slower than the inertia limited vapor bubble growth expressed by the linear dependence by Eq. 9.51. Thus, initially the vapor bubble growth is limited by the inertia, and then the vapor bubble growth becomes limited by the heat transfer. One can estimate the radius and the time when the transition of the two regimes occurs by calculating the intersection of the two curves expressed by the Eqs. 9.51 and 9.55. For typical parameters of acoustic perfluorocarbon droplet vaporization, the vapor bubble growth is heat transfer limited for a typical timescale longer than 1 microsecond (Fig. 9.8).

When the bubble growth is accompanied by bubble oscillations due to the ultrasound forcing, one can observe a phenomenon called rectified heat transfer. Rectified heat transfer is the net effect of the decrease of the heat transfer during the ultrasound half cycle when the vapor bubble surface contracts, and which is lower than the

Fig. 9.8 Radius time dynamics of the inertial and the heat transfer limited vapor bubble growth in superheated liquid. The *curves* are calculated for perfluoropentane liquid (Boiling point $T_b = 29\,°C$) at 35 °C ambient temperature employing the Eqs. 9.51 and 9.55. At $t = 0.52\,\mu s$, the growth becomes limited by the heat transfer as it becomes slower than the growth limited by the inertia
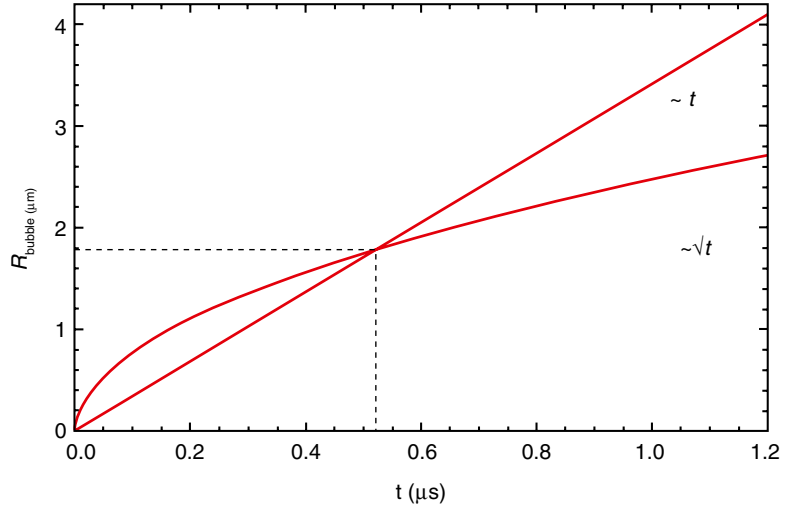
increase of the heat transfer during the second half cycle when the surface expands. Here, two effects come into play; the increment of the bubble wall area during the expansion cycle, and the increment of the temperature gradient. The increment of the temperature gradient can be understood in the following way. Let us consider that the radius of the vapor bubble changes from R_0 to R. The change of the thin thermal boundary layer from δ_0 to δ is then calculated from continuity: $4\pi R^2 \delta = 4\pi R_0^2 \delta_0$. This gives (Prosperetti 2011):

$$\delta = \delta_0 \frac{R_0^2}{R^2} \qquad (9.56)$$

and from the reciprocal relation for the temperature gradient:

$$\frac{\Delta T}{\delta} = \frac{\Delta T}{\delta_0} \frac{R^2}{R_0^2} \qquad (9.57)$$

it can be seen that the temperature gradient increases with the radius squared, R^2, i.e. with the bubble wall area $4\pi R^2$. Thus, the bubble wall area and the temperature gradient will both decrease with R^2 when the radius decreases. However, the net effect is typically positive, meaning that bubble wall oscillations due to the interaction with ultrasound will pump additional heat into the bubble, thereby promoting the phase-conversion process; the larger the bubble oscillation amplitude, the stronger the pumping of additional heat.

9.4.4 Activation Below Boiling Point

After the initiation of droplet vaporization by the focused ultrasound pulse, gas diffuses into the nucleus/vapor bubble during vapor bubble growth as perfluorocarbon droplets dissolve air by an order of magnitude more than water. As was shown before, vapor bubble growth strongly depends on temperature. From both Eq. 9.51 and Eq. 9.55 it follows that the vapor bubble growth is slower when the ambient temperature is lower, whereas the dependence of air diffusion on the temperature is much less pronounced. This means that at low ambient temperatures ($T_\infty \leq T_b$), the air diffusion dynamics becomes comparable to the evaporation processes.

Here, for simplicity, we only show the bubble growth dynamics due to gas diffusion, disregarding the evaporation processes and oscillations of the bubble due to ultrasound forcing. The partial pressure of gas P_g which is in equilibrium with the saturated gas concentration c_s dissolved in the liquid is given by Henry's law:

$$P_g = H c_s \qquad (9.58)$$

We assume that the liquid is at a uniform supersaturated concentration i. The mass flow of gas into the bubble per unit time is:

$$\frac{dm}{dt} = 4\pi R^2 \kappa \left. \frac{\partial c}{\partial r} \right|_{r=R} \qquad (9.59)$$

where κ is the coefficient of diffusivity of the gas in the liquid. If ρ_g is the density of the gas in the bubble, the mass flow can be written as follows:

$$\frac{dm}{dt} = 4\pi R^2 \rho \frac{dR}{dt} \qquad (9.60)$$

One can use the reasonable physical approximation to calculate the gradient of the concentration for a bubble interface, which changes in time by diffusion (Epstein and Plesset 1950):

$$\left.\frac{\partial c}{\partial r}\right|_{r=R} = \left(c_i - c_s\right)\left(\frac{1}{R} + \frac{1}{\sqrt{\pi\kappa t}}\right) \quad (9.61)$$

Substitution of Eqs. 9.60 and 9.61 into Eq. 9.59 gives the radial time dynamics equation for the gas diffusion:

$$\frac{dR}{dt} = \frac{\kappa\left(c_i - c_s\right)}{\rho}\left(\frac{1}{R} + \frac{1}{\sqrt{\pi\kappa t}}\right) \quad (9.62)$$

The gas bubble shrinks when $c_i < c_s$, and grows when $c_i > c_s$. Similar to the rectified heat transfer problem, gas diffusion into the bubble can be promoted due to interaction with ultrasound. This phenomenon is called rectified diffusion and similar relations can be derived as was shown in the previous subsection.

References

Bacon DR (1984) Finite amplitude distortion of the pulsed fields used in diagnostic ultrasound. Ultrasound Med Biol 10:189–195

Biro GP, Blais P, Rosen AL (1987) Peruorocarbon blood substitutes. CRC Critic Rev Oncol Hematol 6:311–374

Bjerknes VFK (1906) Fields of force. Columbia University Press, New York

Blackstock DT (1964) On plane, spherical and cylindrical sound waves of finite amplitude in loss less fluids. J Acoust Soc Am 36:217–219

Carneal CM, Kripfgans OD, Krucker J, Carson PL, Fowlkes JB (2011) A tissue mimicking ultrasound test object using droplet vaporization to create point targets. Pharm Res 58:2013–2025

Church CC (1995) The effects of an elastic solid surface layer on the radial pulsations of gas bubbles. J Acoust Soc Am 97:1510–1521

Cleveland R, Hamilton M, Blackstock DT (1996) Time-domain modeling of finite amplitude sound in relaxing fluids. J Acoust Soc Am 99:3312–3318

de Jong N, Emmer M, Chin CT, Bouakaz A, Mastik F, Lohse D, Versluis M (2007) Compression-only behavior of phospholipid-coated contrast bubbles. Ultrasound Med Biol 33:653–656

Epstein PS, Plesset MS (1950) On the stability of gas bubbles in liquid-gas solutions. J Chem Phys 18:1505–1509

Fabiilli ML, Haworth KJ, Sebastian IE, Kripfgans OD, Carson PL, Fowlkes JB (2010a) Delivery of chlorambucil using an acoustically-triggered perfluoropentane emulsion. Ultrasound Med Biol 36:1364–1375

Fabiilli ML, Lee JA, Kripfgans OD, Carson PL, Fowlkes JB (2010b) Delivery of water-soluble drugs using acoustically triggered perfluorocarbon double emulsions. Ultrasound Med Biol 27:2753–2765

Giesecke T, Hynynen K (2003) Ultrasound-mediated cavitation thresholds of liquid perfluorocarbon droplets in vitro. Ultrasound Med Biol 29:1359–1365

Gramiak R, Shah PM (1968) Echocardiography of the aortic root. Invest Radiol 3:356–366

Hamilton M, Morfey C (2008) Model equations. In: Hamilton MF, Blackstock DT (eds) Nonlinear acoustics. Acoustical Society of America, Melville, pp 41–63

Hamilton M, Tjotta JN, Tjotta S (1985) Nonlinear effects in the farfield of a directive sound source. J Acoust Soc Am 78:202–216

Hart TS, Hamilton MF (1988) Nonlinear effects in focused sound beams. J Acoust Soc Am 84:1488–1496

Kamakura T, Ishiwata T, Matsuda K (2000) Model equation for strongly focused finite amplitude sound beams. J Acoust Soc Am 107:3035–3046

Karshafian R, Bevan PD, Williams R, Samac S, Burns PN (2009) Sonoporation by ultrasound-activated microbubble contrast agents: effect of acoustic exposure parameters on cell membrane permeability and cell viability. Ultrasound Med Biol 35:847–860

Klibanov AL (2006) Microbubble contrast agents: targeted ultrasound imaging and ultrasound-assisted drug-delivery applications. Invest Radiol 41:354–362

Kripfgans OD, Fowlkes JB, Miller DL, Eldevik OP, Carson PL (2000) Acoustic droplet vaporization for therapeutic and diagnostic applications. Ultrasound Med Biol 26:1177–1189

Kuznetsov VP (1971) Equation of nonlinear acoustics. Sov Phys Acoust 16:467–470

Lee YS, Hamilton MF (1995) Time-domain modeling of pulsed finite-amplitude sound beams. J Acoust Soc Am 97:906–917

Lee D, Pierce A (1995) Parabolic equation development in recent decade. J Comput Acoust 3:95–173

Leighton TG (1994) The acoustic bubble. Academic, London

Lindner JR (2004) Microbubbles in medical imaging: current applications and future directions. Nat Rev Drug Discov 35:527–533

Long DM, Multer FK, Greenburg AG, Peskin GW, Lasser EC, Wickham WG, Sharts CM (1978) Tumor imaging with x-rays using macrophage uptake of radiopâque fluorocarbon emulsions. Surgery 84:104–112

Marmottant P, van der Meer SM, Emmer M, Versluis M, de Jong N, Hilgenfeldt S, Lohse D (2005) A model for large amplitude oscillations of coated bubbles accounting for buckling and rupture. J Acoust Soc Am 118:3499–3505

Minnaert M (1933) On musical air-bubbles and sounds of running water. Philos Mag 16:235–248

Neppiras EA, Noltingk BE (1951) Cavitation produced by ultrasonics: theoretical conditions for the onset of cavitation. Proc Phys Soc B 64:1032–1038

Noltingk BE, Neppiras EA (1950) Cavitation produced by ultrasonics. Proc Phys Soc B 63:674–685

Overvelde M (2010) Ultrasound contrast agents: dynamics of coated bubbles. PhD thesis, University of Twente

Overvelde M, Garbin V, Sijl J, Dollet B, de Jong N, Lohse D, Versluis M (2010) Nonlinear shell behavior of phospholipid-coated microbubbles. Ultrasound Med Biol 36:2080–2092

Plesset MS (1949) The dynamics of cavitation bubbles. J Appl Phys 16:277–282

Poritsky H (1952) The collapse or growth of a spherical bubble or cavity in a viscous fluid. Proceedings of the first US National Congress on Applied Mechanics, ASME, New York, pp 813–821

Prosperetti A (2011) Advanced mathematics for applications. Cambridge University Press, Cambridge, UK/New York

Rapoport NY, Gao Z, Kennedy A (2007) Multifunctional nanoparticles for combining ultrasonic tumor imaging and targeted chemotherapy. J Natl Cancer Inst 99:1095–1106

Rapoport NY, Kennedy AM, Shea JE, Scaife CL, Nam KH (2009) Controlled and targeted tumor chemotherapy by ultrasound-activated nanoemulsions/microbubbles. J Control Release 138:268–276

Rayleigh L (1917) On the pressure development in a liquid during the collapse of a spherical cavity. Philos Mag 32:94–98

Reznik N, Shpak O, Gelderblom E, Williams R, de Jong N, Versluis M, Burns P (2013) The efficiency and stability of bubble formation by acoustic vaporization of submicron perfluorocarbon droplets. Ultrasonics 53:1368–1376

Schad KC, Hynynen K (2010) In vitro characterization of perfluorocarbon droplets for focused ultrasound therapy. Phys Med Biol 55:4933–4947

Shpak O, Kokhuis T, Luan Y, Lohse D, de Jong N, Fowlkes B, Fabiilli M, Versluis M (2013a) Ultrafast dynamics of the acoustic vaporization of phase-change microdroplets. J Acoust Soc Am 134:1610–1621

Shpak O, Stricker L, Versluis M, Lohse D (2013b) The role of gas in ultrasonically driven vapor bubble growth. Phys Med Biol 58:2523–2535

Shung KK (2006) Diagnostic ultrasound: imaging and blood flow measurements. CRC Press, Boca Raton

Szabo TL (2004) Diagnostic ultrasound, imaging, inside out. Academic, New York

Szabo TL, Clougherty F, Grossman C (1999) Effects on nonlinearity on the estimation of in situ values of acoustic output parameters. Ultrasound Med Biol 18:33–42

Unger EC, Porter T, Culp W, Labell R, Matsunaga T, Zutshi R (2004) Therapeutic applications of lipid-coated microbubbles. Adv Drug Deliv Rev 59:1291–1314

Unger EC, Hersh E, Vannan M, Matsunaga TO, McCreery T (2009) Local drug and gene delivery through microbubbles. Prog Cardiovasc Dis 41:45–54

Varslot T, Taraldsen G (2005) Computer simulation of forward wave propagation in soft tissue. IEEE Trans Ultrason Ferroelectr Freq Control 52:1473–1482

Westervelt P (1963) Parametric acoustic array. J Acoust Soc Am 52:535–537

Williams R, Wright C, Cherin E, Reznik N, Lee M, Gorelikov I, Foster FS, Matsuura N, Burns PN (2013) Characterization of submicron phase-change perfluorocarbon droplets for extravascular ultrasound imaging of cancer. Phys Med Biol 39:475–489

Zabolotskaya EA, Khokhlov RV (1969) Quasi-plane waves in the nonlinear acoustics of confined beams. Sov Phys Acoust 15:35–40

Zhang P, Porter T (2010) An in vitro study of a phase-shift nanoemulsion: a potential nucleation agent for bubble-enhanced HIFU tumor ablation. Ultrasound Med Biol 36:1856–1866

Zhang M, Fabiilli ML, Haworth KJ, Fowlkes JB, Kripfgans OD, Roberts WW, Ives KA, Carson PL (2010) Initial investigation of acoustic droplet vaporization for occlusion in canine kidney. Ultrasound Med Biol 36:1691–1703